Title

Coded aperture and Compton imaging for the development of 225Ac-based radiopharmaceuticals

Journal

Medical Physics, 50(10)

ISSN

0094-2405

Authors

Frame, Emily
Bobba, Kondapa
Gunter, Donald
et al.

Publication Date

2023-10-01

DOI

10.1002/mp.16717

Received: 1 June 2023 | Revised: 20 July 2023 | Accepted: 30 July 2023

DOI: 10.1002/mp.16717

RESEARCH ARTICLE

MEDICAL PHYSICS

Coded aperture and Compton imaging for the development of ^{225}Ac-based radiopharmaceuticals

Emily Frame[1] | **Kondapa Bobba**[2] | **Donald Gunter**[3,4] | **Lucian Mihailescu**[5] | **Anil Bidkar**[2] | **Robert Flavell**[2,6] | **Kai Vetter**[1,4]

[1]Department of Nuclear Engineering, University of California Berkeley, Berkeley, California, USA

[2]Department of Radiology and Biomedical Imaging, University of California San Francisco, San Francisco, California, USA

[3]Gunter Physics, Inc., Illinois, USA

[4]Applied Nuclear Physics Group, Lawrence Berkeley National Laboratory, Berkeley, California, USA

[5]Ziteo Medical, Inc., Pleasant Hill, California, USA

[6]Department of Pharmaceutical Chemistry, University of California San Francisco, San Francisco, California, USA

Correspondence
Emily Frame, Department of Nuclear Engineering, University of California Berkeley, Berkeley, CA 94502, USA.
Email: eaframe@berkeley.edu

Funding information
National Nuclear Security Administration, Grant/Award Number: DE-NA0003180

Abstract

Background: Targeted alpha-particle therapy (TAT) has great promise as a cancer treatment. Arguably the most promising TAT radionuclide that has been proposed is ^{225}Ac. The development of ^{225}Ac-based radiopharmaceuticals has been hampered due to the lack of effective means to study the daughter redistribution of these agents in small animals at the preclinical stage.

Purpose: The ability to directly image the daughters, namely ^{221}Fr and ^{213}Bi, via their gamma-ray emissions would be a boon for preclinical studies. That said, conventional medical imaging modalities, including single photon emission computed tomography (SPECT) based on nonmultiplexed collimation, cannot be employed due to sensitivity limitations.

Methods: As an alternative, we propose the use of both coded aperture and Compton imaging with the former modality suited to the 218-keV gamma-ray emission of ^{221}Fr and the latter suited to the 440-keV gamma-ray emission of ^{213}Bi.

Results: This work includes coded aperture images of ^{221}Fr and Compton images of ^{213}Bi in tumor-bearing mice injected with ^{225}Ac-based radiopharmaceuticals.

Conclusions: These results are the first demonstration of visualizing and quantifying the ^{225}Ac daughters in small animals through the application of coded aperture and Compton imaging.

KEYWORDS
Actinium-225, coded aperture imaging, Compton imaging, small-animal molecular imaging, targeted alpha-particle therapy

1 | INTRODUCTION

Targeted delivery of alpha-particle-emitting radioisotopes has the potential to be a powerful cancer therapy. Alpha particles have a short range and high linear energy transfer (LET). These characteristics enable highly selective and effective killing of tumors while preserving healthy tissues.[1] In theory, the efficacy of the delivered dose can be enhanced further by employing radioisotopes with decay progeny that also emit alpha particles. One of the more attractive so-called nanogenerators that has been proposed is ^{225}Ac.[2,3] Actinium-225 is a relatively long-lived radioisotope characterized by a half-life of 10 days and undergoes a series of six rapid decays to stable ^{209}Bi as illustrated in Figure 1. The predominant decay pathway of ^{225}Ac yields four alpha particles with contributions from the daughters ^{221}Fr (half-life of 4.90 min), ^{213}Bi (half-life of 45.6 min), and ^{213}Po (half-life of 4.2 μs).

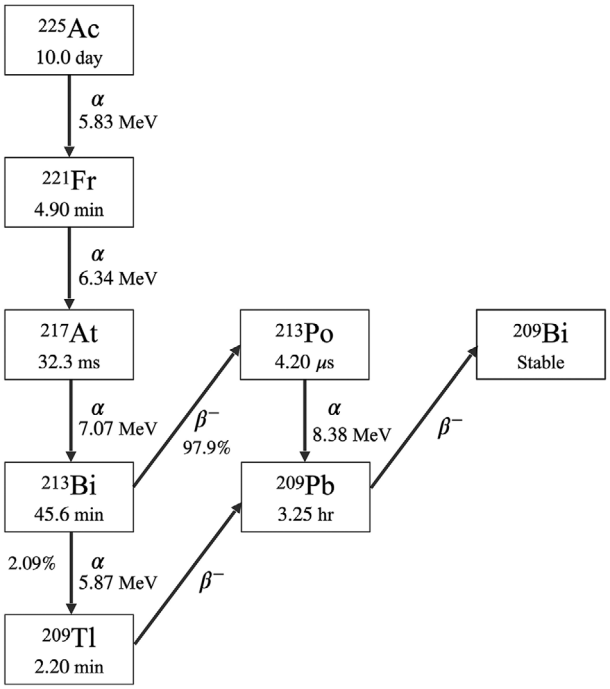

FIGURE 1 Decay scheme of ^{225}Ac.

The progress of ^{225}Ac-based therapies has been hindered despite great promise, primarily due to the lack of effective means to investigate the daughter redistribution.[4] Alpha-particle-emitting daughters, once formed, can possibly break free from the chelator of the radiopharmaceutical due to a high recoil energy and different chemical properties. If the daughters are produced and retained inside the cancerous cells following internationalization, they have the potential to exert a cytotoxic effect. Otherwise, free daughters, generated either on the surface of the cell or during circulation of the radiopharmaceutical, can migrate to healthy organs; thereby resulting in unwanted toxicity. In the case of ^{225}Ac, the redistribution of its longer-lived daughters, namely ^{221}Fr and ^{213}Bi, evokes the most concern.

A typical biodistribution study starts with the administration of the drug under investigation in multiple mice. These mice are subsequently euthanized at different time points. Following each sacrifice, organs are dissected, weighed, and counted (oftentimes using a scintillation counter) to assess the drug accumulation at the given time interval. This entire approach is time-consuming, laborious, and arguably unethical as a large number of animals are required. Furthermore, postmortem analysis prohibits the ability to monitor the biodistribution in individual animals, and organ counting is susceptible to selection bias because unforeseen drug accumulation in unharvested organs is missed.

Overcoming the limitations of invasive biodistribution studies is the primary motivation of small-animal molecular imaging. The noninvasive nature of imaging offers the exciting possibility of evaluating the time-dependent behavior of radiopharmaceuticals in vivo. This enables the collection of a complete set of biodistribution data from a single animal, thereby reducing biological variability and improving data quality. In nuclear medicine, the molecular imaging modalities that have received the greatest attention are positron emission tomography (PET) and single photon emission computed tomography (SPECT). While PET and SPECT have been employed to great effect in the past, there are several considerations that confound their employment in the preclinical evaluation of the ^{225}Ac daughters, which has been the Achilles heel in developing ^{225}Ac-based radiopharmaceuticals.

PET scanners require positron emission, which does not appear in the ^{225}Ac decay scheme. That said, PET can be used to directly image ^{225}Ac agents if the radiopharmaceutical is modified to accommodate a positron-emitting isotope. Consequently, a variety of positron emitters have been investigated as chemical surrogates for ^{225}Ac, including ^{68}Ga, ^{89}Zr, and ^{134}Ce. Cerium-134 is one of the more promising surrogates due to its similar chemical properties and half-life of 75.9 hours, which enables the radiopharmaceutical to be tracked over several days.[5] While PET surrogates can provide valuable insight on the biodistribution of ^{225}Ac agents, they do not provide information about the daughter redistribution.

In principle, SPECT scanners can directly image radionuclides if photon emissions accompany their decay. Indeed, the ^{225}Ac decay scheme includes gamma-ray emissions from the daughters ^{221}Fr and ^{213}Bi. The former daughter emits a gamma ray at 218 keV with a branching ratio of 11.6%, and the latter emits a gamma ray at 440 keV with a branching ratio of 26.1%.

SPECT traditionally employs either a pinhole or parallel-hole collimator, both of which are known to achieve high spatial resolution on a sub-millimeter scale.[6,7] However, collimator-based imagers have a limited photon energy range at which they are effectively operational. At energies above about 300 keV, these systems encounter a decline in response due to the heightened probability of undesired photon transmission through the collimator. This eliminates the potential of effectively utilizing the 440-keV gamma-ray emission of ^{213}Bi. Furthermore, even at energies below 300 keV, conventional SPECT systems have poor imaging sensitivity due to a collimator-driven trade-off between sensitivity and resolution. The sensitivities of conventional, nonmultiplexing collimators rarely exceed values on the order of 10^{-2}.[8] The tradeoff between sensitivity and resolution is not ideal for preclinical studies as these studies involve imaging low doses of radiation on a small scale. In the case of alpha-particle-based radiopharmaceuticals, studies would require particularly low amounts of activity to be injected due to the high efficacy of alpha particles; on the order of 20 kBq in small mice with only a fraction of that reaching the tumor site.[9]

To overcome the limitations of existing small-animal molecular imagers, this work proposes coded aperture and Compton imaging as complementary modalities with the former modality suited to the 218-keV gamma-ray emission of ^{221}Fr and the latter suited to the 440-keV gamma-ray emission of ^{213}Bi. By incorporating the proposed imaging modalities with a PET scanner, which can provide an estimate of the ^{225}Ac biodistribution via positron-emitting surrogates, a full picture of the daughter redistribution can be painted.

At energies below a few hundred keV, coded aperture imagers are advantageous. First introduced by Ables[10] and Dicke,[11] coded apertures decouple the dependence of resolution on sensitivity. The concept behind coded apertures is to increase sensitivity by opening several small pinholes, thereby maintaining resolution. The pinholes are optimally arranged to form the coded aperture or mask. The mask situated in front of a position-sensitive detector collectively constitutes the coded aperture imager. A source within the field-of-view of the imager projects a distinct pattern, unique to its distribution, on the detector plane. The detector measurement is then decoded to determine the gamma-ray distribution.

At energies above a few hundred kiloelectronvolts, Compton imagers become attractive due to their reliance on the dominant interaction mechanism, specifically Compton scattering, at such energies. Additionally, these instruments eliminate the need for a collimator, which would otherwise reduce the sensitivity of the instrument. In general, Compton imaging requires an incident photon to interact at least twice within a single or multiple detectors. By measuring the energies and positions of the first two interactions, a so-called Compton cone can be back-projected into the image space using kinematic relations. The surface of this cone contains all possible positions from which the incident photon could have originated. By acquiring many Compton events and analyzing the intersection of the associated cones, the gamma-ray distribution can be determined.[12,13]

There are several critical design considerations in applying both the coded aperture and Compton imaging concepts to small-animal applications. Because these applications involve weak and small-scale radiation distributions, they require an imager that exhibits both high sensitivity and resolution. To maximize both of these parameters, the distance between the small animal and imager should be minimized. Under such near-field conditions, coded apertures are subject to more severe collimation and magnification effects due to the diverging nature of the incident gamma rays.[14] Design features such as the size, shape, and arrangement of the mask elements must account for these effects to mitigate image artifacts. An in-depth discussion of how our coded aperture was tailored to the near field can be found in Frame et al.[15]

For Compton cameras, one of the more critical design considerations is the detector granularity. This characteristic can be defined as the ability of the imager to discriminate multiple interactions induced by the same incident gamma ray. In other words, a finer granularity corresponds to a smaller volume in which two interactions can be discriminated; thereby increasing the fraction of detected events that are correctly identified. Furthermore, the energy and position resolution of the detectors must be considered as these two parameters strongly impact the attainable image resolution.[16]

The remainder of this article demonstrates the feasibility of imaging the ^{225}Ac daughters in small animals using coded aperture and Compton methods. Section 2 provides an overview of the imaging system, referred to as the Dual-Modality Imager, and evaluates its performance in terms of imaging sensitivity and resolution. Section 3 describes our small-animal experiments and presents coded aperture and Compton images of ^{221}Fr and ^{213}Bi, respectively, in tumor-bearing mice injected with ^{225}Ac agents. A discussion of these results follows in Section 4. Finally, Section 5 provides closing remarks.

2 | IMAGING SYSTEM

2.1 | The Dual-Modality imager

The Dual-Modality Imager is a gamma-ray imaging system that provides both coded aperture and Compton imaging capabilities. This system was not designed for small-animal applications and is merely employed here as a proof-of-concept prototype. The Dual-Modality Imager consists of two high-purity germanium (HPGe) double-sided strip detectors (DSSDs) with three-dimensional (3-D) position sensitivity. The two detectors are enclosed within a single cryostat and positioned with a 10-mm gap between them to optimize the solid angle coverage. Each detector is comprised of a planar HPGe crystal with an active volume of $74 \times 74 \times 15$ mm^3 that is surrounded by 2-mm-wide guard rings to minimize leakage current. On the opposing faces of each detector, there are 37×37 strip electrodes positioned orthogonally with a pitch of 2 mm. This electrode arrangement provides an intrinsic granularity of 1369 2×2-mm^2 pixels.

A custom-made coded aperture is positioned in front of the first detector that faces the source at an adjustable distance. The arrangement of the detector and mask is shown in Figure 2a. The coded aperture is constructed from 2.4-mm-thick tungsten, providing approximately 90% attenuation at 250 keV. The mask consists of 64×64 square elements with each element having a 2×2-mm^2 face. The elements are arranged in a random pattern with a 50% open fraction. The pattern was generated and optimized using a combinatorial search technique.[15]

The combination of the coded aperture and first detector creates the coded aperture imager, while the first and second detectors together form the Compton

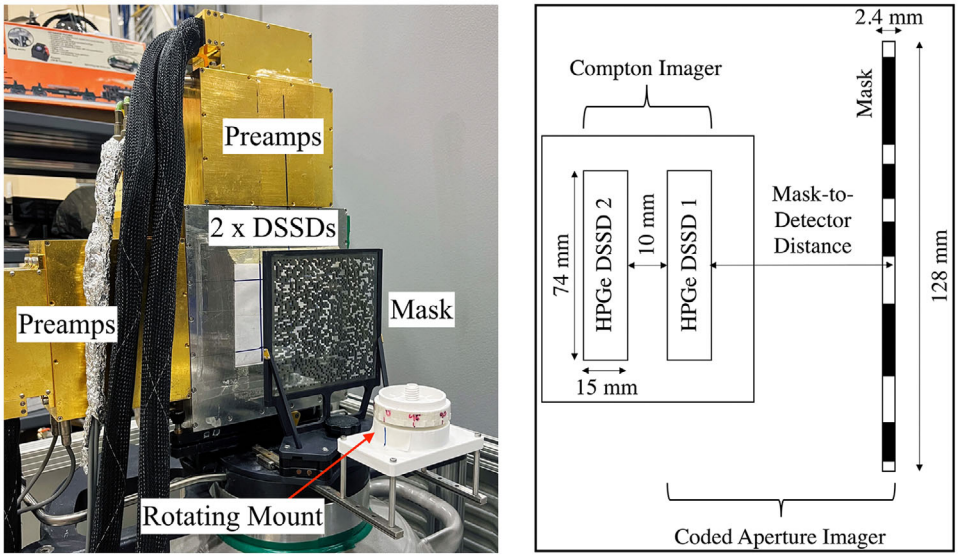

FIGURE 2 (a) The Dual-Modality Imager featuring two DSSDs and a coded aperture. (b) An illustration depicting the configurations of the coded aperture and Compton geometries.[15]

camera, as shown Figure 2b. It is important to note that operating both modalities simultaneously impacts the imaging performance. The presence of the coded aperture results in fewer photons reaching the detector; thereby reducing the Compton sensitivity. Additionally, in the Compton mode, reducing the distance between the source and imager enhances the image resolution. However, with the coded aperture in place, the minimum standoff distance is limited to that between the coded aperture and first detector. Due to these factors, the two modalities are operated separately, with the mask removed in the Compton mode.

In designing a more specialized system for improved sensitivity and resolution, a third detector can be introduced on the opposite side of the mask. In this configuration, the Compton camera would be formed by the original two detectors, and the coded aperture imager would be formed by the mask and newly added third detector. This configuration would allow the source to be positioned in between the two modalities at an optimal distance that maximizes both the sensitivity and resolution of each modality. Additionally, such a design would enable simultaneous use of both modalities without a cost to imaging performance. In the context of this work, simultaneous operation would enable the observation of the ^{221}Fr and ^{213}Bi biodistributions at the same time.

2.2 | Imaging sensitivity

Imaging sensitivity can be defined as the ratio of photons selected for image reconstruction (in cps) to the activity (in MBq) of the source. The sensitivity of the Dual-Modality Imager was determined by acquiring coded aperture and Compton data from an ^{225}Ac-filled microsphere with a well-defined activity. The microsphere with an inner volume of about 40 μL was filled with a mixture of water and ^{225}Ac in secular equilibrium with ^{221}Fr and ^{213}Bi. The total activity was 7.0 kBq at the time of the coded aperture measurement and 6.5 kBq at the time of the Compton measurement.

For the coded aperture measurement, the 7.0 kBq microsphere was positioned in the center of the field-of-view at a distance of 145 mm from the surface of the first detector. We intentionally chose this standoff distance to match that of the small animal in the coded aperture mode. A total of 2700 events were acquired at the 218-keV emission line of ^{221}Fr after 41 min. This equates to a sensitivity of about 160 cps/MBq (0.016%) for ^{221}Fr at a standoff distance of 145 mm.

For the Compton measurement, the 6.5-kBq microsphere was positioned in the center of the field-of-view at a distance of 35 mm from the surface of the first detector. We intentionally chose this standoff distance to match that of the small animal in the Compton mode. A total of 4400 events were acquired at the 440-keV emission line of ^{213}Bi after 75 min. This equates to a sensitivity of about 150 cps/MBq (0.015%) for ^{213}Bi at a standoff distance of 35 mm.

2.3 | Image resolution

Image resolution is strongly controlled at the detector level. For example, the position resolution of the detectors influences both the coded aperture and Compton image resolutions. For all practical purposes, the lateral position resolution of DSSDs in full-width at half-maximum (FWHM) can be approximated as the strip pitch; our DSSDs have a 2-mm pitch. The depth

resolution of our detectors was previously reported to be as good as 0.5 mm in FWHM.[17]

Furthermore, the energy resolution of the detectors exclusively impacts the Compton image resolution. Specifically, the uncertainty in the first energy deposition, of which the finite energy resolution of the detectors is a contributor, propagates to the uncertainty in the Compton cone opening angle. This error propagation blurs the Compton image. Thanks to the favorable detection properties of HPGe, our detectors demonstrate excellent energy resolution, with an average ranging from 0.2 to 0.5% at 662 keV.

Accorsi[14] derives the following expression for the resolution of a coded aperture imager:

$$\delta r_{CA} \approx \left(\frac{1}{m-1}\right)\sqrt{[(m)(w_m)]^2 + w_d^2} \quad (1)$$

where δr_{CA} is the lateral image resolution in FWHM, w_d is the lateral position resolution of the detector, and w_m is the mask pixel width. In our case, w_d and w_m are both 2 mm. The parameter m is the magnification factor defined as

$$m = 1 + \frac{b}{a} \quad (2)$$

where m represents the size ratio of the mask element projection to the mask element itself, a is the normal distance between the source and mask planes, and b is the normal distance between the mask and detector planes.

According to Equation (1), given a fixed coded aperture design, the resolution improves by increasing the magnification factor m. This objective can be achieved by reducing the distance a between the source and mask and/or increasing the distance b between the mask and detector. We intentionally select both a and b to be as small as possible to maximize sensitivity. Given the geometric constraints of the coded aperture and small-animal mounts, we are limited to $a = 95$ mm and $b = 50$ mm so that $m = 1.5$. At this magnification, the coded aperture imager should theoretically achieve a resolution of about 6.9 mm in FWHM.

We validated the theoretical coded aperture resolution by evaluating a back-projected image of a ^{57}Co disc source in the coded aperture mode. The source with a 2-mm active diameter was positioned near the center of the field-of-view at a distance of 95 mm from the mask with the mask positioned at a distance of 50 mm from the detector. Figure 3 shows a linear intensity profile of the back-projection captured at the highest intensity image voxel. This cross-section was fitted with a one-dimensional (1-D) Gaussian model. The Gaussian FWHM was determined to be 6.4 mm. By performing a 1-D deconvolution of the source diameter from the Gaussian FWHM, an estimate of the resolution was obtained. The resolution was calculated to be approximately 6.3 mm, which aligns well with the theoretical value of 6.9 mm.

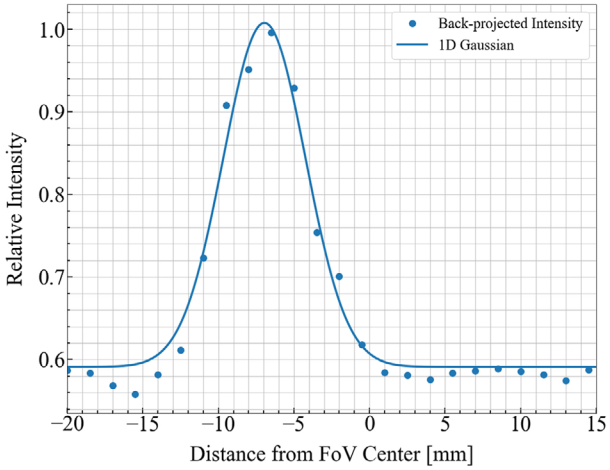

FIGURE 3 Linear intensity profile of a back-projected image of a ^{57}Co disk source with a 2-mm active diameter in the coded aperture mode. The source was positioned near the center of the field-of-view at a magnification of $m = 1.5$. To estimate the image resolution in FWHM, the intensity profile was fitted with a 1-D Gaussian model.

The resolution of a Compton imager can be defined as

$$\delta r_{CI} \approx (2z)\tan\left(\frac{\delta\theta}{2}\right) \quad (3)$$

where δr_{CI} is the lateral image resolution in FWHM, z can be approximated as the normal distance between the source and the detector surface facing the source and $\delta\theta$ is the angular resolution.[18] In Compton imaging, $\delta\theta$ is governed by uncertainties in the energies and positions of interaction. The former uncertainty is governed by the finite energy resolution of the detectors and Doppler broadening, while the latter uncertainty is governed by the finite position resolution of the detectors.

To determine the Compton angular resolution $\delta\theta$, a standard approach is to generate an angular resolution metric (ARM) distribution. The ARM metric can be defined as the angular distance between the Compton cone and known source position. We produced ARM distributions from simulated (Geant4) data at both 440 and 662 keV. We also generated an ARM distribution from experimental data at 662 keV to demonstrate the consistency between experiment and simulations. For the experiment, we collected Compton data at 662 keV from a ^{137}Cs disc source with a 2-mm active diameter. The source was positioned at a distance of 200 mm from the surface of the first detector. We intentionally chose a large standoff distance to ensure that the imager perceived the source as a point-like object.

Figure 4 displays the ARM distributions, which have been fitted using a 1-D Lorentzian model. The FWHM of the Lorentzian serves as an estimate of the angular resolution $\delta\theta$. The simulated and experimental ARM distributions at 662 keV are consistent, showing FWHMs

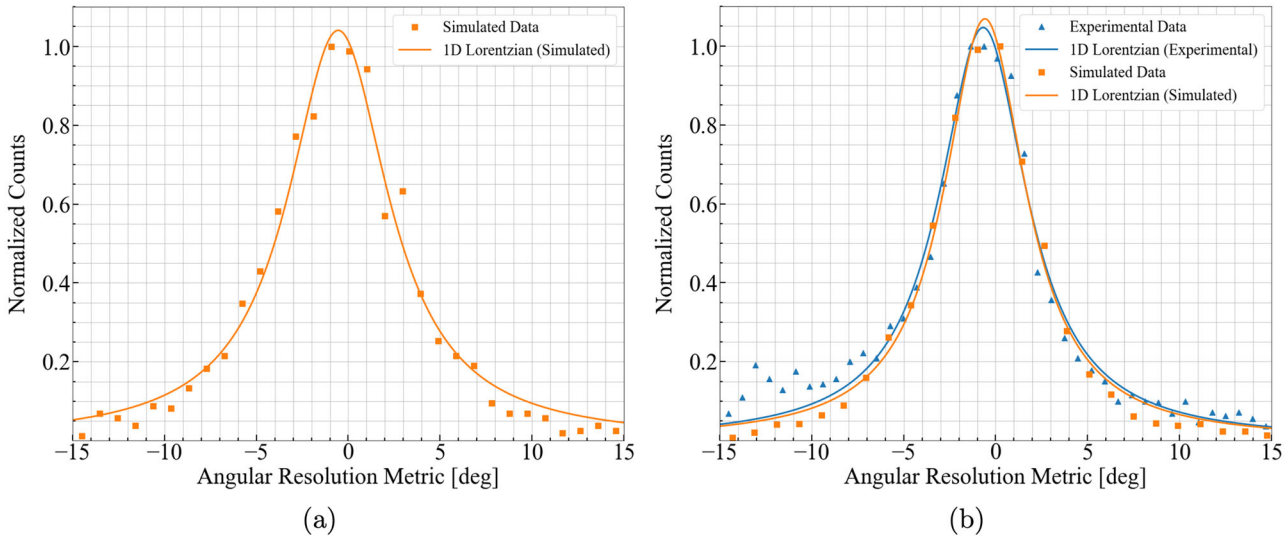

FIGURE 4 ARM distributions at (a) 440 keV from simulated data only and (b) 662 keV from both simulated and experimental data. To estimate the angular resolution in FWHM, each ARM distribution was fitted with a 1-D Lorentzian model.

of 5.4° and 5.5°, respectively. Thus, we can have confidence in the simulated ARM distribution at 440 keV, which exhibits a FWHM of 6.7°. Note the angular resolution improves with increased energy. This should be expected. At higher energies, the effects of Doppler broadening and energy resolution are less impactful, and photons exhibit greater penetration that results in longer lever arms. All of these factors contribute to a more well-defined Compton cone.

Based on Equation (3), angular errors are amplified by the distance z between the source and the detector. Consequently, it is preferable to position the source in close proximity to the detector to minimize these errors. Given the geometric constraints of the detector and small-animal containments, the minimum allowable standoff distance is 35 mm. At this distance for a 440-keV source, the Compton imager should theoretically achieve a resolution of about 4.1 mm in FWHM.

3 | EXPERIMENTS AND RESULTS

3.1 | Phantom filled with ^{225}Ac

This section presents a coded aperture image of ^{221}Fr and Compton image of ^{213}Bi in an ^{225}Ac-filled phantom. These images provide quantification factors for the subsequent small-animal images. Figure 5a displays the phantom, featuring a cylindrical body with an inner diameter of 40 mm and inner height of 82 mm. Inside are three micro-hollow spheres of various sizes. The inner diameters of the spheres are about 4.3, 6.2, and 7.8 mm, with corresponding inner volumes of about 40, 125, and 250 μL, respectively.

Figure 5b shows the configuration of the spheres inside the phantom. The sphere centers are positioned in a triangular fashion on the same (x, z) transverse plane. The large and medium spheres are positioned with a separation distance of 25.4 mm between their centers. Additionally, the small sphere is situated at a distance of 18.0 mm from the centers of both the large and medium spheres.

The phantom body was filled entirely with water, while the spheres were each filled completely with the same mixture of water and ^{225}Ac in secular equilibrium with ^{221}Fr and ^{213}Bi. The activity concentration was 0.53 kBq/μL at the time of preparation. Given this concentration, the smallest sphere contained 22 kBq, the medium sphere contained 67 kBq, and the largest sphere contained 133 kBq.

Figure 5c displays the experimental setup of the phantom in the coded aperture mode at 2 days post-preparation. By the time of this measurement, the activities inside the spheres had decayed to 19, 58, and 117 kBq in order of the smallest to largest sphere. The phantom was positioned centrally on a rotating mount, with the rotation axis located at a distance of 95 mm from the mask. The mask itself was positioned at a distance of 50 mm from the surface of the first detector. In this configuration, the coded aperture imager is expected to achieve a theoretical resolution of approximately 6.9 mm in FWHM. The mount was rotated in increments of 45°. For each viewing angle, an average of 3.1×10^4 events was acquired at the 218-keV emission line of the daughter ^{221}Fr after a duration of 30 min. The total imaging time amounted to 4 h.

Figure 5d displays the experimental setup of the phantom in the Compton mode at 14 days post-preparation. By the time of this measurement, the

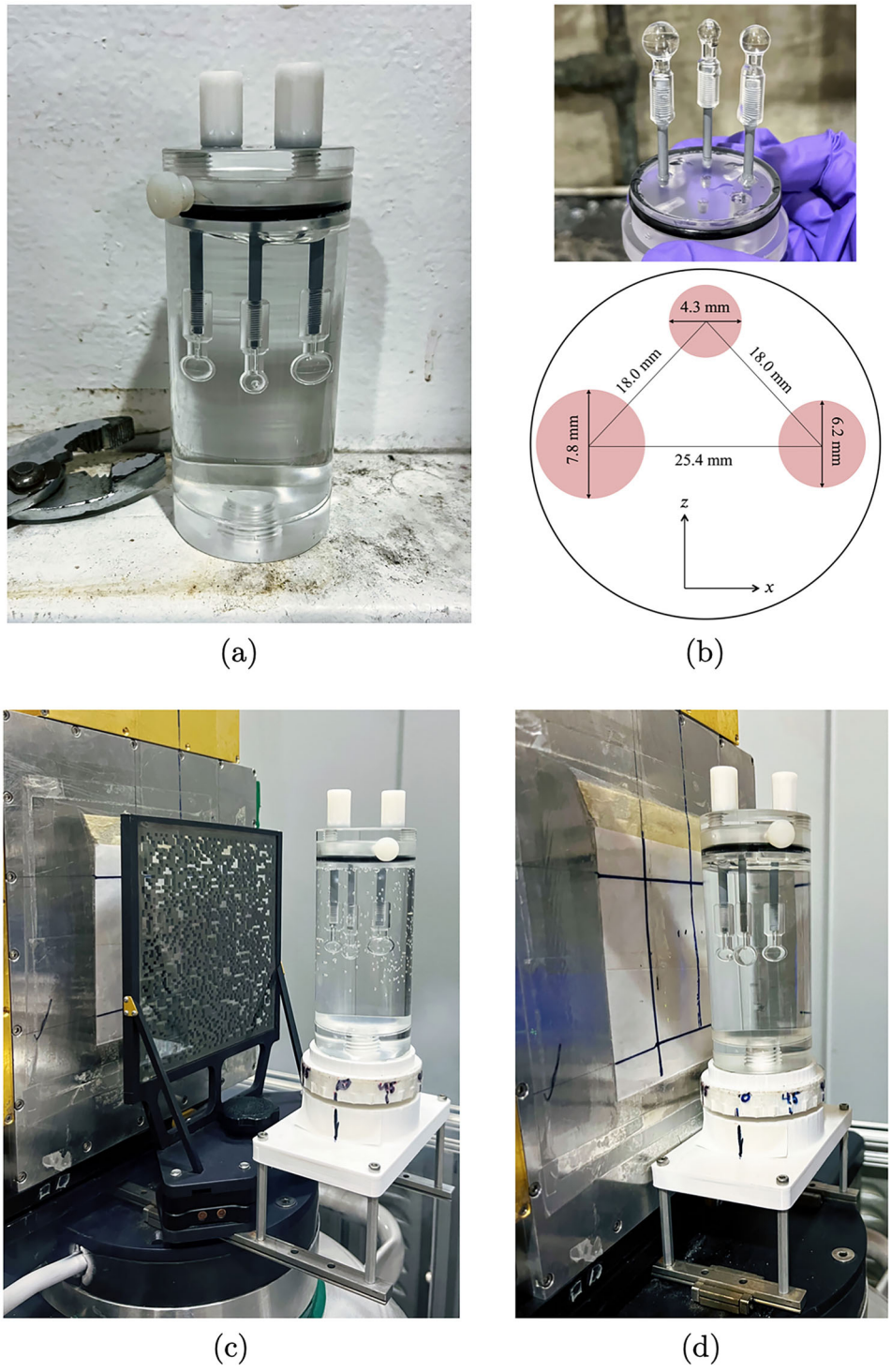

FIGURE 5 (a) The phantom features a cylindrical body. (b) Within the phantom, there are three micro-hollow spheres with inner diameters of 4.3, 6.2, and 7.8 mm. These spheres are positioned in a triangular arrangement on the same transverse plane (x, z). (c) The experimental setup of the phantom in the coded aperture mode, with the phantom and mask positioned at a distance of 145 and 50 mm, respectively, from the surface of the first detector. (d) The experimental setup of the phantom in the Compton mode, with the phantom positioned at a distance of 55 mm from the surface of the first detector.

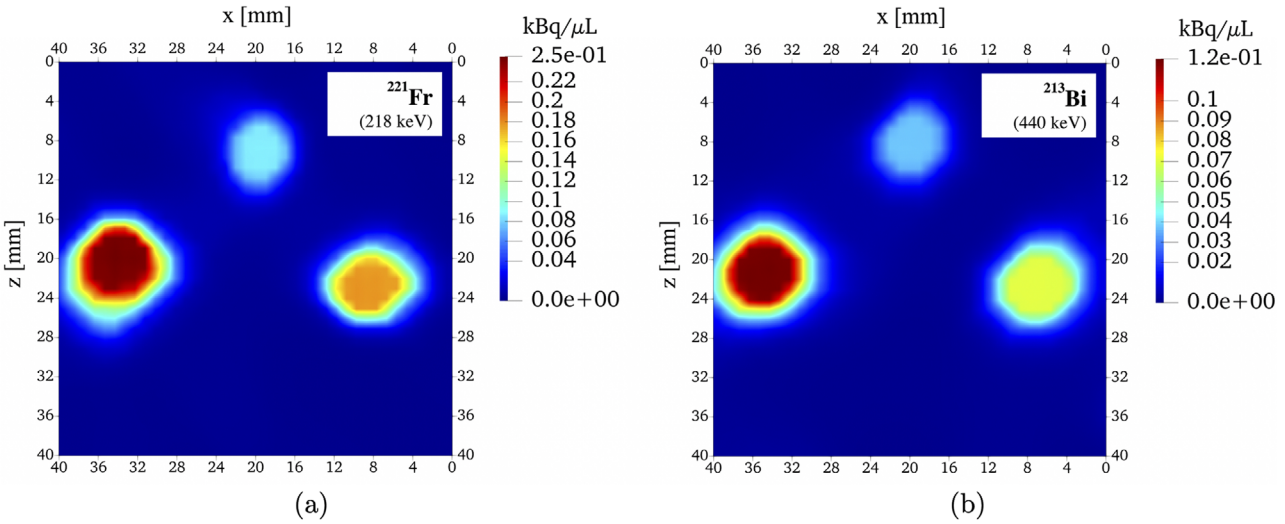

FIGURE 6 Two-dimensional transverse (x, z) slices of the ^{225}Ac-filled phantom. (a) Coded aperture image generated from a total of 2.5×10^5 events at 218 keV. (b) Compton image generated from a total of 6.7×10^4 events at 440 keV.

activities inside the spheres had decayed to 8, 25, and 51 kBq in order of the smallest to largest sphere. The phantom was positioned centrally on a rotating mount. For maximum resolution and sensitivity, the mount was positioned as close as possible to the detector with the rotation axis located at a distance of 55 mm from the surface of the first detector. In this configuration, the Compton imager is expected to achieve a theoretical resolution of approximately 6.4 mm in FWHM at 440 keV. The mount was rotated in increments of 45°. For each viewing angle, an average of 8.4×10^3 events was acquired at the 440-keV emission line of the daughter ^{213}Bi after a duration of 30 min. The total imaging time amounted to 4 h.

The restriction of the imager location to eight positions (associated with 45° source rotations) is significantly less than what is typically used in standard SPECT imaging. The reason for requiring fewer rotations is that both the coded aperture and Compton modalities offer parallax, allowing depth information to be obtained from a single viewing angle. In contrast, a standard gamma camera does not possess this capability.

The phantom was reconstructed in 3-D from the coded aperture and Compton data at the 218- and 440-keV emission lines, respectively. The reconstruction was performed using maximum-likelihood expectation-maximization (ML-EM) with total variation (TV) as described by Frame.[19] The coded aperture and Compton images were both generated from all eight projections after 250 iterations. Figure 6 shows the central (x, z) transverse slices of the phantom images.

The intensity scales of the images are expressed in units of activity per volume (kBq/μL). To obtain the activity units, quantification factors Q were determined based on the coded aperture and Compton images of the phantom:

$$Q = \frac{I}{(A)(T)\left(\frac{1}{R^2}\right)\exp\left[-(\mu_{H2O})(X)\right]} \tag{4}$$

where I is the sum total of intensity in the three reconstructed microspheres as determined by the ML-EM algorithm, A is the known activity of the three microspheres at the time of measurement, T is the imaging time, R represents the normal distance from the center of the phantom to the surface of the first detector, and the exponential $\exp[-(\mu_{H2O})(X)]$ corrects for photon attenuation in water. The attenuation distance X is assumed to be equivalent to the radius of the phantom body. The water linear attenuation coefficient μ_{H2O} is evaluated at 218 keV for the coded aperture modality and 440 keV for the Compton modality. The coded aperture and Compton quantification factors Q are assumed constant and are applied to the subsequent small-animal images of ^{221}Fr and ^{213}Bi, respectively. By simply plugging Q into a rearranged Equation (4), the activity A, now considered an unknown, can be determined.

It is worth noting that the intensity scale of the coded aperture image is approximately twice as high as that of the Compton image. This disparity is due to the former measurement being conducted 12 days prior to the latter measurement. Moreover, a slight discrepancy can be observed in the gamma-ray distributions depicted in the coded aperture and Compton images. This dissimilarity can be attributed to the distinct resolution profiles inherent to each modality.

Table 1 summarizes the activities and diameters of the three reconstructed microspheres in Figure 6. In the

TABLE 1 Activities and diameters of the coded aperture and Compton reconstructed microspheres in Figure 6 versus the ground truth. Diameters are reported as FWHM.

	Coded Aperture			Compton		
True Dia. [mm]	Recon. Dia. [mm]	True Act. [kBq]	Recon. Act. [kBq]	Recon. Dia. [mm]	True Act. [kBq]	Recon. Act. [kBq]
4.3	7.2	19	19	6.8	8	9
6.2	7.9	58	56	7.6	25	25
7.8	8.1	117	119	7.9	51	50

coded aperture image, the sum totals of activity in each reconstructed sphere are 19, 56, and 119 kBq in order of the smallest to largest sphere, respectively. These values are consistent with the actual activities at the time of measurement. Furthermore, the extents of the reconstructed spheres at the central linear cross-section are 7.2, 7.9, and 8.1 mm in FWHM in order of the smallest to largest sphere, respectively.

In the Compton image, the sum totals of activity in each reconstructed sphere are 9, 25, and 50 kBq in order of the smallest to largest sphere, respectively. These values are consistent with the actual activities at the time of measurement. Furthermore, the extents of the reconstructed spheres at the central linear cross-section are 6.8, 7.6, and 7.9 mm in FWHM in order of the smallest to largest sphere, respectively.

The phantom images in Figure 6 are representative of results that are attainable with our current imaging system. In reality, the three microspheres have an equal activity concentration, but different sizes. Given an ideal system, the reconstructed spheres would display equal intensity with the appropriate sizes for each sphere. Because of the limited spatial resolution of the Dual-Modality Imager, the three reconstructed spheres appear to be roughly the same size. Nonetheless, the reconstruction produces three spheres with the correct total activity, but distributed over the larger volumes. Consequently, the smaller two spheres appear less intense, rather than smaller, in the images. Better spatial resolution would solve this problem.

3.2 | Tumor-bearing mice injected with ^{225}Ac

Five- to 6-week-old male athymic mice were implanted subcutaneously with 5×10^6 22Rv1 prostate cancer cells into the right flank at the Molecular Imaging Laboratory at the University of California San Francisco (UCSF). Approximately 3–5 weeks after tumor implantation, the mice were injected with either ^{225}Ac-Macropa-PEG8(7)-YS5 or ^{225}Ac-DOTA-YS5 via the tail vein. The mice were then euthanized at different time intervals to evaluate the tumor-targeting specificity. The synthesis and biodistribution results for each of these ^{225}Ac agents have been reported published separately.[20,21] Furthermore, these radioimmunotherapy agents are similar to previously reported ^{89}Zr-labeled PET radiopharmaceuticals that target the antigen CD46, which is highly expressed on the surface of prostate and other cancers.[22]

We received two of the mice, hereinafter labeled as A and B, from the UCSF study. Mice A and B were injected with 20 kBq of ^{225}Ac-Macropa-PEG8(7)-YS5 and ^{225}Ac-DOTA-YS5, respectively. Following injection, mice A and B were euthanized at 2 and 4 days, respectively. The mice were each housed in a 50-mL falcon tube and stored at a temperature of $-7°$C when not in use.

To assess the potential of using coded aperture and Compton imaging for evaluating the daughter redistribution of ^{225}Ac in small animals, mice A and B were imaged via both modalities. The coded aperture and Compton images are overlaid with CT scans. CT imaging was performed separately from the gamma-ray measurements using a MILabs U-CT system; thus, the co-registration is not precise. The following describes the experiments and results in more detail.

Figure 7a displays the experimental setup of mouse A in the coded aperture mode at 2 days post-injection. The falcon tube containing mouse A was positioned centrally on a rotating mount, with the rotation axis located at a distance of 95 mm from the mask. The mask itself was positioned at a distance of 50 mm from the surface of the first detector. In this configuration, the coded aperture imager is expected to achieve a theoretical resolution of approximately 6.9 mm in FWHM. The mount was rotated in increments of 45°. For each viewing angle, an average of 4.2×10^3 events was acquired at the 218-keV emission line of ^{221}Fr after a duration of 60 min. The total imaging time amounted to 8 h.

Figure 7b displays mouse A in the Compton mode at 4 days post-injection. To maximize the imaging sensitivity and resolution, the falcon tube was positioned as close as possible to the detector in an upright orientation. The central axis of the tube was situated at a distance of 35 mm from the surface of the first detector. In this configuration, the Compton imager is expected to achieve a theoretical resolution of approximately 4.1 mm in FWHM. The falcon tube was rotated by hand in 45° increments. For each viewing angle, an

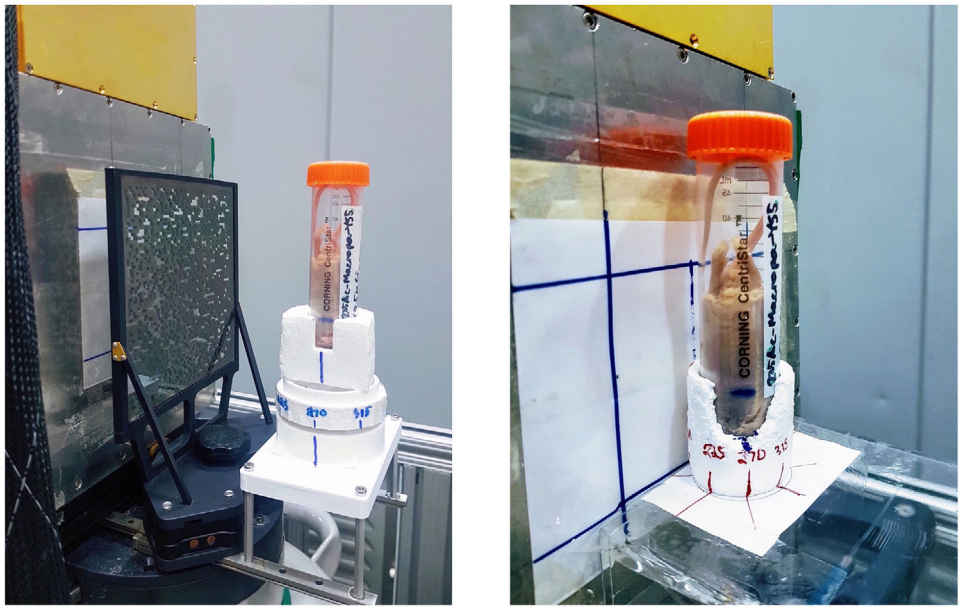

(a) (b)

FIGURE 7 Experimental setup of mouse A in the (a) coded aperture mode at a source-to-detector distance of 145 mm with a mask-to-detector distance of 50 mm and (b) Compton mode at a source-to-detector distance of 35 mm.

average of 4.1×10^3 events was acquired at the 440-keV emission line of ^{213}Bi after a duration of 75 min. The total imaging time amounted to 10 h.

In the case of mouse B, the coded aperture and Compton experimental setups were identical to those shown in Figure 7. The coded aperture measurement of mouse B took place at 4 days post-injection, and data were acquired for a duration of 120 min at each 45° viewing angle. The total imaging time amounted to 16 h, and an average of 3.9×10^3 events was acquired at the 218-keV emission line of ^{221}Fr for each rotation. The Compton measurement of mouse B took place at 6 days post-injection, and data were acquired for a duration of 70 min at each 45° viewing angle. The total imaging time amounted to 9.3 h, and an average of 1.6×10^3 events was acquired at the 440-keV emission line of ^{213}Bi for each rotation.

Note that mouse B required double the imaging time of mouse A to have sufficient statistics for coded aperture imaging. Despite mice A and B being administered the same amount of activity, the count rate observed in mouse B was about a factor of two lower. This should be expected. Mouse B was sacrificed 2 days later than mouse A; thereby excreting more of the radiopharmaceutical.

Using ML-EM with TV, the two mice were reconstructed in 3-D from the coded aperture and Compton data at the 218-keV emission line of ^{221}Fr and 440-keV emission line of ^{213}Bi, respectively. The coded aperture and Compton images were both generated from all eight projections after 250 iterations. Figures 8b,c and 9b,c show the maximum intensity projections (MIP) of the gamma-ray images of mice A and B, respectively. These images are fused with a CT MIP. Furthermore, Figures 8e,f and 9e,f show coronal slices of the gamma-ray images of mice A and B, respectively. These images are fused with a coronal CT image. The quantification factor, determined from the phantom measurements in Section 3.1, was applied to each image so that the intensity scale is in units of percent injected activity per cubic centimeter (%IA/cc). Additionally, the intensity scales are decay corrected to the day of injection.

Note that the coded aperture and Compton images exhibit no clear distinction between the central organs. This observation can be attributed in part to the restricted resolution capabilities of the imaging modalities; and thus going forward, improvements in resolution should be a priority. Furthermore, due to the limited and distinct resolution profiles of the coded aperture and Compton modalities, we cannot provide a concrete explanation for the discrepancies between the small-animal images of ^{221}Fr and ^{213}Bi. The variations are most likely imaging artifacts, but there could also be a physiological explanation.

Ex vivo biodistribution analyses of mice A and B were performed at 9 and 11 days post-injection, respectively, to validate the gamma-ray images. Major organs were harvested, weighed, and counted using a Hidex Automated Gamma Counter. Table 2 displays the activity estimates of ^{221}Fr and ^{213}Bi in the various organs as determined by the biodistribution analyses and

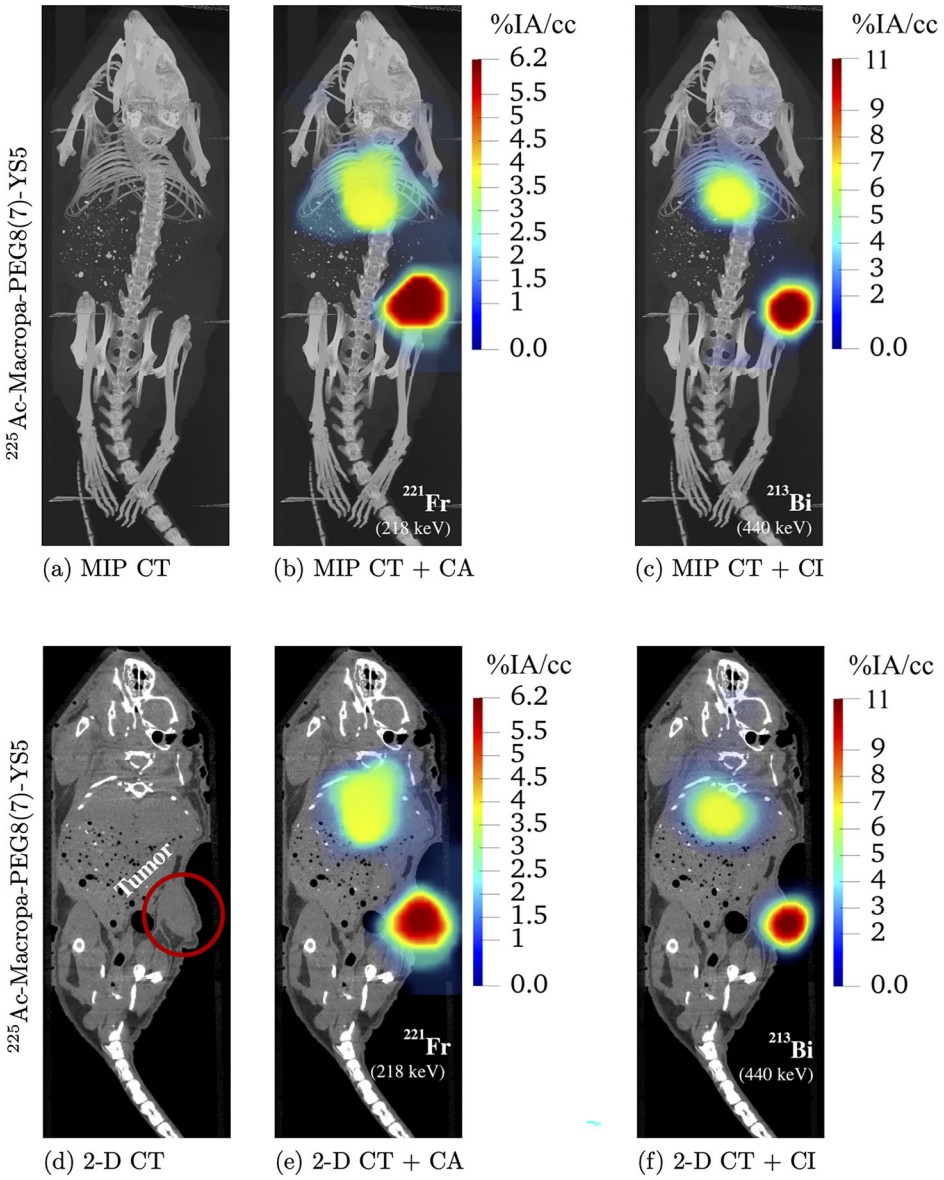

FIGURE 8 (a) CT MIP of mouse A fused with the (b) coded aperture (CA) and (c) Compton (CI) MIPs. (d) CT coronal slice of mouse A fused with coronal slices of the (e) CA and (f) CI images. The CA image was generated from a total of 3.4×10^4 events at 218 keV, and the CI image was generated from a total of 3.3×10^4 events at 440 keV. The intensity scales are decay corrected to the day of injection.

gamma-ray images. All activities are decay corrected to the day of injection.

4 | DISCUSSION

The ability to visualize and quantify the ^{225}Ac daughters, namely ^{221}Fr and ^{213}Bi, in small animals would facilitate the advancement of ^{225}Ac-based radiopharmaceuticals. These radiopharmaceuticals have shown potential as a promising cancer treatment, as demonstrated in previous studies.[3] This is the first time that ^{221}Fr and ^{213}Bi have been imaged via their gamma-ray emissions in mice using coded aperture and Compton methods. That said, a previous work by de Swart et al.[23] imaged ^{213}Bi via its 440-keV gamma-ray emission in a mouse using a multipinhole SPECT imager. The multipinhole system was designed to maximize resolution for energies up to 600 keV at the expense of imaging sensitivity. Indeed, de Swart presents high-resolution images of ^{213}Bi agents in mice. However, these results are based on an injected activity of 3 MBq. This activity is 150 times greater than that required of preclinical targeted alpha-particle therapy (TAT) studies. In contrast, we present images of mice with injected activities of 20 kBq.

Other works have already proposed a Compton camera for the preclinical evaluation of the daughter ^{221}Bi;[24,25] however, none have demonstrated the feasibility of this modality via experimentation. The most recent study by Caravaca et al.[25] simulates the response

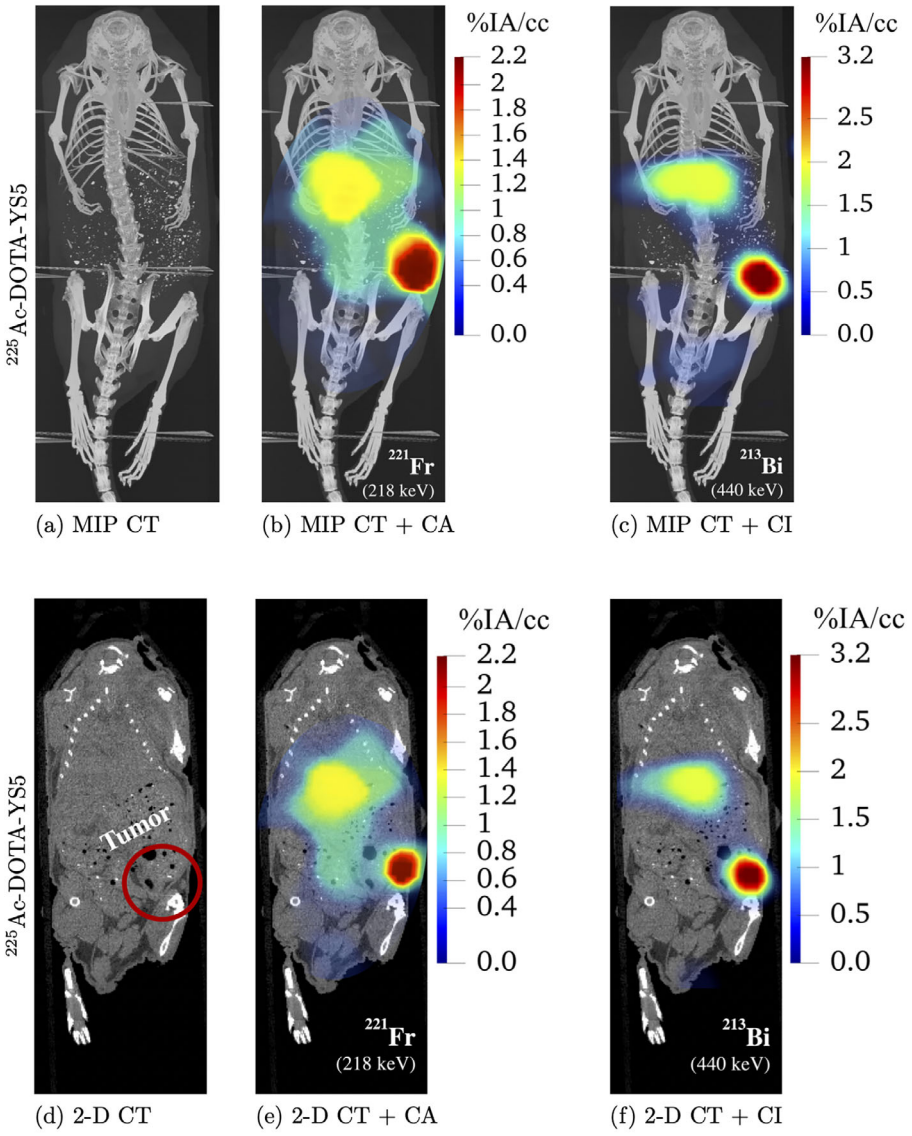

FIGURE 9 (a) CT MIP of mouse B fused with the (b) coded aperture (CA) and (c) Compton (CI) MIPs. (d) CT coronal slice of mouse B fused with coronal slices of the (e) CA and (f) CI images. The CA image was generated from a total of 3.1×10^4 events at 218 keV, and the CI image was generated from a total of 1.2×10^4 events at 440 keV. The intensity scales are decay corrected to the day of injection.

of a Compton imager based on CZT. The simulated results show the ability of the Compton camera to image ^{213}Bi via its 440-keV gamma-ray emission in a mouse phantom injected with 20 kBq. Furthermore, Caravaca proposes a proximity imager to image ^{221}Fr via its 218-keV gamma-ray emission and presents simulated results. The findings indicate that the proximity modality has the capability to image ^{221}Fr in a point-like phantom at a standoff distance of 1 mm. Nevertheless, in small-animal imaging, the standoff distances typically correspond to the size of the animal body. At such distances, proximity imaging has not been demonstrated to have reasonable resolution.

Previous works have proposed and employed coded apertures for small-animal imaging,[26] but as far as we know, this work is the first to recommend a coded aperture for imaging ^{221}Fr via its 218-keV emission in small animals. Other analogous collimator-based systems have been employed to image ^{221}Fr.[27,28] These studies show preliminary images of phantoms, but none have demonstrated sufficient sensitivity to image activities as low as 20 kBq.

A study by Wang et al.[22] presents both a biodistribution analysis and PET image of a [^{89}Zr]DFO-YS5 agent in a mouse implanted with the same 22Rv1 prostate cancer cells as the mice presented here. The ^{89}Zr agent is similar to the ^{225}Ac-Macropa-PEG8(7)-YS5 and ^{225}Ac-DOTA-YS5 agents injected in mice A and B, respectively. The results in Wang provide an estimate of the ^{225}Ac biodistribution, which can serve as a foundation for assessing the daughter redistribution.

The biodistribution analysis of the [^{89}Zr]DFO-YS5 agent shows a tumor uptake of 14.5 ± 3.2 %IA/g at

TABLE 2 Activity estimates in major organs of (a) mouse A and (b) mouse B as determined by the biodistribution (BioD) and coded aperture (CA) and Compton (CI) images. The biodistribution data are displayed as both activity in units of Becquerel (Bq) and percent injected activity per gram (%IA/g). The image data are displayed as activity (Bq). The central organs encompass the liver, heart, and lungs. All reported values are decay corrected to the day of injection.

(a) Mouse A injected with 20 kBq of ^{225}Ac-Macropa-PEG8(7)-YS5 and sacrificed at 2 days post-injection.

		BioD		CA	CI
	Wt.	^{221}Fr	^{213}Bi	^{221}Fr	^{213}Bi
Organ	[g]	[Bq, %IA/g]	[Bq, %IA/g]	[Bq]	[Bq]
Tumor	0.300	1152, 19.2	1064, 17.8	1219	1035
Liver	0.597	786, 6.58	706, 5.91	–	–
Heart	0.252	246, 4.89	239, 4.74	–	–
Lungs	0.174	176, 5.06	195, 5.59	–	–
Kidneys	0.327	192, 2.93	210, 3.21	–	–
Central Organs	1.02	1208, 5.90	1140, 5.57	1298	1220

(b) Mouse B injected with 20 kBq of ^{225}Ac-DOTA-YS5 and sacrificed at 4 days post-injection.

		BioD		CA	CI
	Wt.	^{221}Fr	^{213}Bi	^{221}Fr	^{213}Bi
Organ	[g]	[Bq, %IA/g]	[Bq, %IA/g]	[Bq]	[Bq]
Tumor	0.186	217, 5.84	198, 5.33	299	242
Liver	0.731	240, 1.64	238, 1.63	–	–
Heart	0.153	75, 2.46	71, 2.33	–	–
Lungs	0.199	122, 3.06	125, 3.14	–	–
Kidneys	0.423	111, 1.32	94, 1.11	–	–
Central Organs	1.08	437, 2.02	434, 2.00	610	575

4 days post-injection and less than 5 %IA/g in all other organs. In this work, the biodistribution of mouse A shows 19.2 %IA/g of ^{221}Fr and 17.8 %IA/g of ^{213}Bi in the tumor at 2 days post-injection and less than 7 %IA/g of both isotopes in all other organs (Table 2 a). The biodistribution of mouse B shows significantly lower uptake. The tumor has 5.84 %IA/g of ^{221}Fr and 5.33 %IA/g of ^{213}Bi at 4 days post-injection, and all other organs have less than 4 %IA/g of both isotopes (Table 2 b). The lower uptake could be related to a number of factors, including biological variations and a suboptimal tumor dissection. In regards to the latter, if the harvested tumor also included adjacent skin or muscle, then the uptake would appear less. This is a likely cause given that organs were found damaged upon dissection.

Similarly to the biodistribution analyses, the PET image of ^{89}Zr (Figure 3a in Wang) and the gamma-ray images of ^{221}Fr and ^{213}Bi (Figures 8 and 9) show the highest uptake in the tumor and noticeable uptake in the central organs. The PET image of ^{89}Zr has an intensity scale that ranges up to 20 %IA/cc, whereas the coded aperture and Compton images have intensity scales with maximums between 2 %IA/cc and 11 %IA/cc. The intensity variations between the PET image of ^{89}Zr and the gamma-ray images of ^{221}Fr and ^{213}Bi might be indicative of the daughters redistributing, but for now, such claims cannot be made. The discrepancies might also be a result of biological variations associated with using both different mice and radioimmunotherapy agents. A more definitive explanation can be attributed to the differing resolution profiles of the imaging modalities. The coded aperture and Compton imagers possess resolutions that are approximately five and three times lower, respectively, compared to a small-animal PET scanner. As a result, the intensities in the coded aperture and Compton images are distributed across a greater number of image voxels. Going forward, the resolutions of the two modalities will need to match that of PET so that the daughter redistribution can be properly assessed.

The consistency between the biodistribution analyses and coded aperture and Compton images contributes to the credibility of this work. In the case of mouse A (Table 2 a), the biodistribution shows the highest uptake in the tumor with a total activity accumulation of about 1152 Bq of ^{221}Fr and 1064 Bq of ^{213}Bi. This is consistent with the coded aperture and Compton images, which show total accumulations of about 1219 Bq of ^{221}Fr and 1035 Bq of ^{213}Bi, respectively. Furthermore, the biodistribution of mouse A shows significant uptake in the liver, heart, and lungs. In combination, these three organs show total activity accumulations of about 1208 Bq of ^{221}Fr and 1140 Bq of ^{213}Bi. This is consistent with the coded aperture and Compton images, which show accumulations of about 1298 Bq of ^{221}Fr and 1220 Bq of ^{213}Bi, respectively, in the central region of the mouse.

In the case of mouse B (Table 2 b), the biodistribution shows the highest uptake in the tumor with a total activity accumulation of about 217 Bq of ^{221}Fr and 198 Bq of ^{213}Bi. This is consistent with the coded aperture and Compton images, which show total accumulations of about 299 Bq of ^{221}Fr and 242 Bq of ^{213}Bi, respectively. Furthermore, the biodistribution of mouse B shows significant uptake in the liver, heart, and lungs. In combination, these three organs show total activity accumulations of about 437 Bq of ^{221}Fr and 434 Bq of ^{213}Bi. The coded aperture and Compton images show accumulations of about 610 Bq of ^{221}Fr and 575 Bq of ^{213}Bi, respectively, in the central region. Note the biodistribution of mouse B shows significantly lower activities in the central organs compared to the images. This discrepancy can be partially explained by a suboptimal biodistribution analysis. Upon dissection of mouse B, several organs were found to be damaged and may not have been fully harvested.

While the quantification estimates from the biodistribution analyses and small-animal images are in close agreement, these estimates have no associated uncertainties. Going forward, a more advanced and

comprehensive methodology for quantifying activities and estimating the corresponding uncertainties should be developed.

Another area of improvement is on image resolution. The current system could not discriminate the central organs, for example, liver, heart, and lungs, given the 6.9- and 4.1-mm resolutions of the coded aperture and Compton modalities, respectively. Going forward, the image resolution can be improved significantly by reducing the strip pitch of the detectors and the size of the mask elements. For example, by employing DSSDS with a 0.5-mm strip pitch and a mask with elements to match, the coded aperture resolution could be enhanced by approximately 75% at the existing magnification of 1.5, and the Compton resolution could improve by about 40% at a photon energy of 440 keV and standoff distance of 35 mm. Further enhancements to the coded aperture resolution can be achieved by increasing the magnification factor. If a magnification of 3 was realized, then the coded aperture resolution would improve by an additional 50%. The Compton resolution can be improved further by decreasing the standoff distance. If a distance of 20 mm were realized, then the Compton resolution would improve by an additional 40%.[19]

Improvements to imaging sensitivity should also be a priority moving forward, so that the imaging time can be reduced and organs with relatively low uptake (e.g., kidneys) can be resolved. Currently, the coded aperture modality has a sensitivity of about 160 cps/MBq (0.016%) for ^{221}Fr at a standoff distance of 145 mm, and the Compton modality has a sensitivity of about 150 cps/MBq (0.015%) for ^{213}Bi at a standoff distance of 35 mm. These values can be improved by increasing the solid angle coverage of the detectors. For example, by simply reducing the standoff distance by half and adding four panels of each modality around the small animal, the sensitivity of both modalities would increase by a factor of 16. Further sensitivity improvements can be realized by mitigating information loss in signal processing. This can be achieved by reducing the granularity of the detectors via a smaller strip pitch and employing more advanced signal processing algorithms.

5 | CONCLUSION

The notable contribution of this work lies in the utilization of coded aperture and Compton imaging principles for the preclinical assessment of the daughter redistribution of ^{225}Ac-based radiopharmaceuticals. Up until now, there has been a lack of effective methods to investigate the daughter redistribution in small animals, which is an integral step towards clinical approval. This work presented coded aperture images of ^{221}Fr and Compton images of ^{213}Bi in both an ^{225}Ac-filled phantom and tumor-bearing mice injected with ^{225}Ac agents. Activity estimates were extracted from the small-animal images and validated by *ex vivo* biodistribution analyses. These results are the first demonstration of visualizing and quantifying the ^{225}Ac daughters in small animals through the application of coded aperture and Compton imaging and serve as a stepping stone for future radiopharmaceutical studies.

ACKNOWLEDGMENTS

This research was funded by the Department of Energy National Nuclear Security Administration through the Nuclear Science and Security Consortium under Award Number DE-NA0003180. The authors would like to thank Ross Barnowski of the Department of Nuclear Engineering at UC Berkeley for his contribution in the development of the Dual-Modality Imager, Rebecca Abergel and Lee Bernstein of the Department of Nuclear Engineering at UC Berkeley for their valuable insight on TAT, Bin Liu of the Department of Anesthesia at UCSF for developing the YS5 antibody, Ian Baldridge of EH&S at UC Berkeley for delivering the mice, Ryan Tang and Youngho Seo of the Department of Radiology and Biomedical Imaging at UCSF for providing the CT data, and finally the US Department of Energy Isotope Program for providing the ^{225}Ac.

CONFLICT OF INTEREST STATEMENT

The authors declare no conflicts of interest.

REFERENCES

1. Pouget JP, Navarro-Teulon I, Bardiès M, et al. Clinical radioimmunotherapy-the role of radiobiology. *Nat Rev Clin Oncol*. 2011;8(12):720-734.
2. McDevitt MR, Scheinberg DA. Ac-225 and her daughters: the many faces of Shiva. *Cell Death Differ*. 2002;9(6):593-594.
3. Kratochwil C, Bruchertseifer F, Giesel FL, et al. 225Ac-PSMA-617 for PSMA-targeted α-radiation therapy of metastatic castration-resistant prostate cancer. *J Nucl Med*. 2016;57(12):1941-1944.
4. De Kruijff RM, Wolterbeek HT, Denkova AG. A critical review of alpha radionuclide therapy-how to deal with recoiling daughters. *Pharmaceuticals*. 2015;8(2):321-336.
5. Bailey TA, Mocko V, Shield KM, et al. Developing the 134Ce and 134La pair as companion positron emission tomography diagnostic isotopes for 225Ac and 227Th radiotherapeutics. *Nat Chem*. 2021;13(3):284-289.
6. McElroy DP, MacDonald LR, Beekman FJ, et al. Performance evaluation of A-SPECT: a high resolution desktop pinhole SPECT system for imaging small animals. *IEEE Trans Nucl Sci*. 2002;49(5):2139-2147.
7. Van Der Have F, Vastenhouw B, Ramakers RM, et al. U-SPECT-II: an ultra-high-resolution device for molecular small-animal imaging. *J Nucl Med*. 2009;50(4):599-605.
8. Van Audenhaege K, Van Holen R, Vandenberghe S, Vanhove C, Metzler SD, Moore SC. Review of SPECT collimator selection, optimization, and fabrication for clinical and preclinical imaging. *Med Phys*. 2015;42(8), 4796-4813.
9. Moroz A, Wang Y-H, Sharib JM, et al. Theranostic Targeting of CUB Domain Containing Protein 1 (CDCP1) in pancreatic cancer treating cancer by targeting CUB Domain Containing Protein 1. *Clin Cancer Res*. 2020;26(14):3608-3615.
10. Ables JG. Fourier transform photography: a new method for X-ray astronomy. *Proc Astron Soc Aust*. 1968;1:172-173.

11. Dicke RH. Scatter-hole cameras for x-rays and gamma rays. *The astroPhysical Journal*. 1968;153:L101.
12. Todd RW, Nightingale JM, Everett DB. A proposed γ camera. *Nature*. 1974;251(5471):132-1343.
13. Phillips GW. Gamma-ray imaging with Compton cameras. *Nucl Instrum Methods Phys Res, Sect B*. 1995;99(1-4):674-677.
14. Accorsi R. *Design of a Near-field Coded Aperture Cameras for High-resolution Medical and Industrial Gamma-ray Imaging*. PhD thesis. Massachusetts Institute of Technology; 2001.
15. Frame E, Ross B, Donald G, Lucian M, Kai V. A dual-modality volumetric gamma-ray imager for near-field applications. *IEEE Trans Nucl Sci*. 2022;69(12):2343-2359.
16. Nurdan TC, Nurdan K, Brill AB, Walenta AH. Design criteria for a high energy Compton camera and possible application to targeted cancer therapy. *J Instrum*. 2015;10(7):C07018.
17. Chivers DH. *Pulse Shape Parameterization and Signal Decomposition for High Sensitivity Compton Imaging Using High-purity Germanium Double-sided Strip Detectors*. PhD thesis. University of California, Berkeley; 2008.
18. Hautiere N. Visible edges thresholding: a HVS based approach. In: *18th International Conference on Pattern Recognition*. 2006;2:155-158.
19. Frame E. *Three-Dimensional Coded Aperture and Compton Gamma-Ray Imaging for Near-field Applications*. PhD thesis. University of California, Berkeley; 2022.
20. Bobba K, Bidkar A, Wang S, et al. Influence of short PEG linkers on biodistribution of 225Ac-Macropa-YS5, an immunoconjugate for treating CD46 expressing cancer. *Nucl Med Biol*. 2022;108:S53.
21. Bidkar A, Wang S, Bobba KN, et al. Treatment of prostate cancer with CD46 targeted 225Ac alpha particle radioimmunotherapy. *Clin Cancer Res*. 2023;29(10):1916-1928.
22. Wang S, Li J, Hua J, et al. Molecular imaging of prostate cancer targeting CD46 using ImmunoPETMolecular imaging of prostate cancer targeting CD46. *Clin Cancer Res*. 2021;27(5):1305-1315.
23. De Swart J, Chan HS, Goorden MC, et al. Utilizing high-energy γ-photons for high-resolution 213Bi SPECT in mice. *J Nucl Med*. 2016;57(3):486-492.
24. Yoon C, Jo S, Cho Y, Kim N, Lee T. Estimate of the 225Ac radioactive isotope distribution by means of DOI Compton imaging in targeted alpha radiotherapy: A Monte Carlo simulation. *J Korean Phys Soc*. 2020;76(10):954-960.
25. Caravaca J, Huh Y, Gullberg GT, et al. Compton and proximity imaging of 225Ac in vivo with a CZT gamma camera: a proof of principle with simulations. *IEEE Trans Radiat Plasma Med Sci*. 2022;6(8):904-915.
26. Accorsi R, Gasparini F, Lanza RC. A coded aperture for high-resolution nuclear medicine planar imaging with a conventional Anger camera: experimental results. *IEEE Trans Nucl Sci*. 2001;48(6):2411-2417.
27. Robertson A, Ramogida CF, Rodríguez-Rodríguez C, Blinder S, Kunz P, Sossi V, Schaffer P. Multi-isotope SPECT imaging of the 225Ac decay chain: feasibility studies. *Phys Med Biol*. 2017;62(11):4406.
28. Cai L, Zannoni EM, Nie X, Meng L-J. Hyperspectral single photon imaging of targeted alpha therapy. *J Nucl Med*. 2021;62:1141.

How to cite this article: Frame E, Bobba K, Gunter D, et al. Coded aperture and Compton imaging for the development of ^{225}Ac-based radiopharmaceuticals. *Med Phys*. 2023;50:6454–6468.
https://doi.org/10.1002/mp.16717